RSC Applied Interfaces

ROYAL SOCIETY OF CHEMISTRY

PAPER

View Article Online
View Journal | View Issue

Cite this: *RSC Appl. Interfaces*, 2025, **2**, 1220

Cathodically electrodeposited nitrogen-doped carbon dot–acrylic nanocomposite coatings: a dual-function corrosion barrier and real-time corrosion sensor†

Sushmit Sen, [a] Amrita Chatterjee, [a] Keshav Dev,[ab] Shakshi Bhardwaj[a] and Pradip K. Maji *[a]

Received 1st March 2025,
Accepted 5th May 2025

DOI: 10.1039/d5lf00058k

rsc.li/RSCApplInter

In this study, nitrogen-doped carbon dots (N-CDs) were successfully incorporated into an acrylic-based cathodic electrodeposition (CED) coating to develop an advanced nanocomposite system. The N-CDs, synthesized *via* a hydrothermal method, were directly integrated into the electrodeposition bath without requiring isolation, simplifying the fabrication process. The resulting coatings demonstrated enhanced mechanical strength, improved adhesion, and superior corrosion resistance compared to conventional acrylic coatings, increasing the impedance by a factor of 10^4. In addition, the fluorescence quenching property of N-CDs in the presence of Al^{3+} was utilized for real-time corrosion monitoring. A simple pH-paper-like sensor was fabricated using N-CDs as an ink, enabling naked-eye detection of aluminum corrosion through a "turn-off" fluorescence mechanism. This dual functionality—both as a corrosion barrier and a corrosion sensor—presents a novel approach to material protection and monitoring. This study highlights the potential of N-CDs in the development of next-generation intelligent coatings for structural materials.

1. Introduction

Corrosion significantly undermines the longevity and integrity of metallic structures, not only leading to economic losses,[1] but also making the metallic structures unsafe.[2] Consequently, substantial efforts have been dedicated to extending the durability of metals through effective protective measures.[3] Among these, polymer coatings have emerged as a versatile, cost-effective, and widely adopted solution, offering excellent electrical insulation, barrier properties, and adhesion to substrates. These attributes enable polymer coatings to shield metallic surfaces from corrosive agents and oxygen. Consequently, the development of eco-friendly, safe, and non-toxic anticorrosive polymer coatings remains a critical research focus.

Cathodic electrodeposition (CED) coatings represent a notable advancement in this field, addressing limitations of anodic electrodeposition coatings such as film discoloration and dissolution of the substrate. In the CED process, positively charged resins deposit on the cathode under an applied electric current, producing defect-free, uniform coatings even on complex substrate geometries. Acrylic resins are particularly suited for CED coatings due to their superior gloss, adhesion, and mechanical hardness.[4] For instance, Gong *et al.* synthesized acrylic resins *via* copolymerization of methyl methacrylate (MMA), styrene (St), butyl acrylate (BA), hydroxypropyl methacrylate (HPMA), and dimethylaminoethyl methacrylate (DMAEMA), neutralized the resin with acetic acid, and achieved thin, uniform coatings.[5] Similarly, Haghi *et al.* prepared cationic acrylic resins by varying the ratio of 2-ethylhexyl acrylate (EHA), MMA, and *tert*-butyl acrylate (TBA), using tertiary amino methacrylate (DMAEMA) and hydroxy methacrylate (HEMA) functionalities. These resins, crosslinked with alkylated melamine formaldehyde, demonstrated exceptional anticorrosive properties with a dry film thickness of around 20 ± 2 μm.[6] Collectively, these studies establish acrylic resins as promising candidates for CED coatings.[7–10]

Despite their advantages, the corrosion inhibition performance of acrylic coatings remains limited. To address this, researchers have incorporated nanofillers such as carbon dots (CDs) to enhance anti-corrosive capabilities.[11–13] For

[a] *Department of Polymer and Process Engineering, Indian Institute of Technology Roorkee, Saharanpur Campus, Saharanpur-247001, India.*
E-mail: pradip@pe.iitr.ac.in; Tel: +91 7895965010
[b] *Department of Chemistry, Indian Institute of Technology Roorkee, Roorkee-247667, India*

† Electronic supplementary information (ESI) available. See DOI: https://doi.org/10.1039/d5lf00058k

example, Zhao *et al.* demonstrated that CDs could effectively inhibit corrosion on steel substrates,[14] while Wang *et al.* reported improved anticorrosive performance of epoxy coatings *via* nitrogen-doped carbon dots (N-CDs).[15]

Other studies further corroborate the efficacy of CDs and N-CDs as corrosion inhibitors.[16–18] However, current approaches often involve labor-intensive steps to isolate N-CDs in the solid form before their integration into coatings, a bottleneck for scalability. Furthermore, traditional application methods like brush or dip coating fail to achieve uniform, defect-free coverage on intricately designed substrates.[4]

Thus, the CED coating technique has been introduced to solve these problems. But, to date, the possibility of depositing N-CDs *via* electrodeposition as a nanocomposite coating has not been highlighted and it remains an important research gap in the advancement of coating technology.

To overcome these challenges, this study pioneers the electrodeposition of N-CDs as nanocomposite fillers in an acrylic-based CED coating. N-CDs were synthesized *via* a solvothermal method and incorporated directly into the resin bath without requiring their isolation as a powder, thereby eliminating time-consuming preparatory steps. The resulting acrylic/N-CD nanocomposite coatings exhibit enhanced mechanical strength and anticorrosive performance, marking a significant step forward in the advancement of CED coating technologies.

2. Details of the experiments

2.1. Materials

The monomers methyl methacrylate (MMA), tertiary butyl acrylate (*t*-BA), hydroxypropyl methacrylate (HPMA), and dimethylaminoethyl methacrylate (DMAEMA) were purchased from TCI Chemicals, India. The initiator 2,2′-azobis(2-methylpropionitrile) (AIBN) was purchased from HiMedia, India. No further purification of the reagents was carried out.

The aluminum (Al) substrates and water soluble crosslinker Cyamel were very kindly supplied by M/S SBL Specialty Coatings, India.

2.2. Synthesis of N-CDs

The synthesis of the N-CDs was done following the method used by Song *et al.*[19] 80 mmol of acrylic acid and 80 mmol of *O*-phenylene diamine were dissolved completely in 60 ml of deionized (DI) water and sonicated for 15 min for complete dissolution. The mixture was then transferred into polytetrafluorethylene (PTFE) autoclaves and kept at 180 °C for 24 h. A dark brownish-orange solution was obtained after cooling to room temperature. The solutions were utilized as is.

Some of the solvent was cast on a Petri-dish for film formation to be used in X-ray spectroscopy (XPS). Some of the solution was diluted to 0.0001 wt% and sonicated using a probe sonicator to be utilized to remove any agglomeration. The sonicated solution was drop-cast onto a 200 mesh size copper TEM-grid using a micropipette.[20]

2.3. Resin preparation

The polymer used as the binder for the coating was synthesized through solution polymerization *via* addition polymerization. A three-neck reactor equipped with a nitrogen inlet, condenser, and a dropping funnel was used to carry out the reaction, as shown in Fig. 1a. A magnetic stirrer ensured uniform mixing of the reactants. Initially, 0.3 g of AIBN was dissolved in 25 mL ethyl acetate and stirred continuously until the reaction temperature reached 80 °C. 15 g MMA, 10 g *t*-BA, 5 g each of DMAEMA and HPMA, and another 0.3 g of AIBN were dissolved in 25 mL ethyl acetate and added dropwise to the reactor over a period of 2.5 hours. After the monomer addition was complete, the reaction temperature was raised to 90 °C and the reaction was continued for an additional 2 hours.

2.4. Preparation of the N-CD-CED composite coating bath

5 g of the synthesized resin was mixed with 0.5 g of acetic acid for the neutralization of the tertiary amine to NH_4^+. The neutralized resin was then dissolved in water as per the recipe in Table 1. After stirring for 15 min, at 60 °C, the water-soluble diisocyanate crosslinker, Cyamel, and the N-CD solution were added as per the given recipe. The mixture was further stirred for 20 min at the same temperature for complete homogenization. The nanocomposite baths were named as Ac0NCD, Ac0.5NCD, Ac1NCD, and Ac1.5NCD depending on the amount (ml) of N-CD solution present in the bath preparation.

2.5. Substrate preparation and coating application

The aluminum panels were supplied as square specimens in the dimensions of 2.5 cm × 2.5 cm × 0.3 mm. Using 600 pieces of water sandpaper, the panels were sanded and cleaned by acetone rub and dried under ambient conditions.

The resin bath was prepared as per section 2.4. The Al substrate and the stainless-steel counter electrode were dipped in the resin bath. The cathode and the anode were connected to the negative and the positive terminals of a rectifier as seen in Fig. 2. A voltage of 40 V was applied for 30 s for the deposition of the nanocomposite onto the Al cathode. After the completion of the deposition, the coated substrate was washed with DI water for the removal of excess material.

The coated samples were put in a hot air oven at 80 °C for 30 min for the drying process. The temperature was raised to 120 °C for 30 min more for the curing of the coatings.

Some of the resin bath was solution cast to form a thin film for the FTIR, thermal, and SEM analysis.

2.6. Characterization

2.6.1. Characterization of the polymer. Fourier transform infrared (FTIR) spectroscopy (PerkinElmer FTIR, UATR Spectrum Two) was utilized to analyze the chemical structure of the polymers using the attenuated total reflectance (ATR)

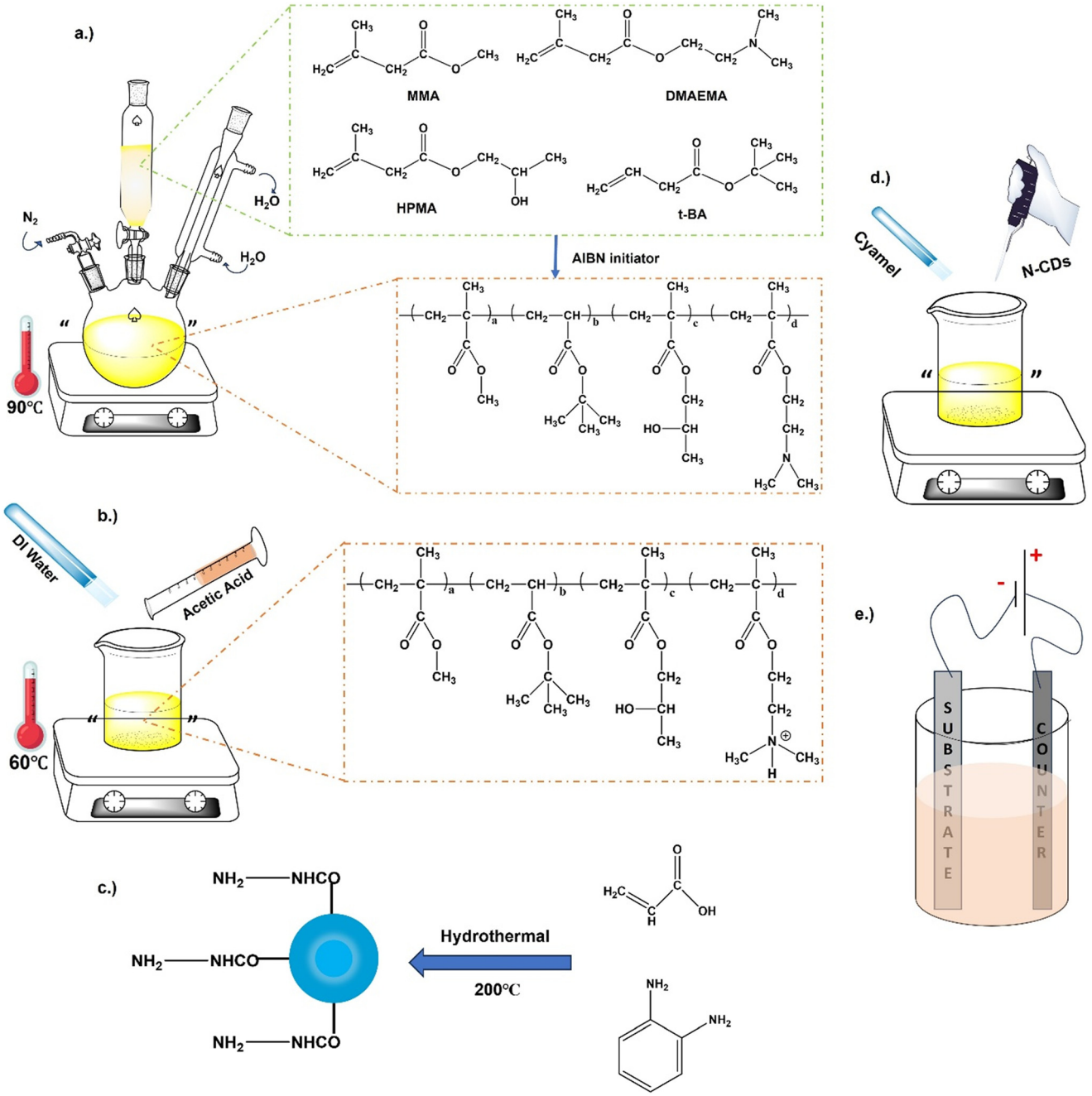

Fig. 1 Representation of a.) formation of the acrylic co-polymer from various acrylic monomers; b.) neutralizing the tertiary amine of the polymer with acid to make the polymer cathodic in nature; c.) synthesis of N-CDs *via* a hydrothermal method; d.) addition of a crosslinker and N-CDs for the preparation of the resin bath; e.) set-up for the electrodeposition of the polymer coating on the metal substrate.

mode. The measurements were conducted with a resolution of 4 cm^{-1} over a spectral range of 4000 cm^{-1} to 400 cm^{-1}.

Table 1 Recipe for the preparation of the resin bath

Sample name	Resin	Water	Acid	Crosslinker	N-CD solution
Ac0NCD	5 g	20 ml	0.5 g	0.2 g	0 ml
Ac0.5NCD	5 g	19.5 ml	0.5 g	0.2 g	0.5 ml
Ac1NCD	5 g	19 ml	0.5 g	0.2 g	1 ml
Ac1.5NCD	5 g	18.5 ml	0.5 g	0.2 g	1.5 ml

The thermal properties of the nanocomposite as well as the pristine polymer were evaluated by thermogravimetric analysis (TGA) and differential thermogravimetry (DTG) using a HITACHI TG/DT 7200. ~15 mg of the sample was kept in a sample platinum pan and was heated to the temperature range of 25 °C to 500 °C, and the temperature was raised at a rate of 10 °C min^{-1}.

2.6.2. Characterization of the N-CDs. The synthesized N-CDs were characterized for the confirmation of their morphology and structure. Transmission electron microscopy

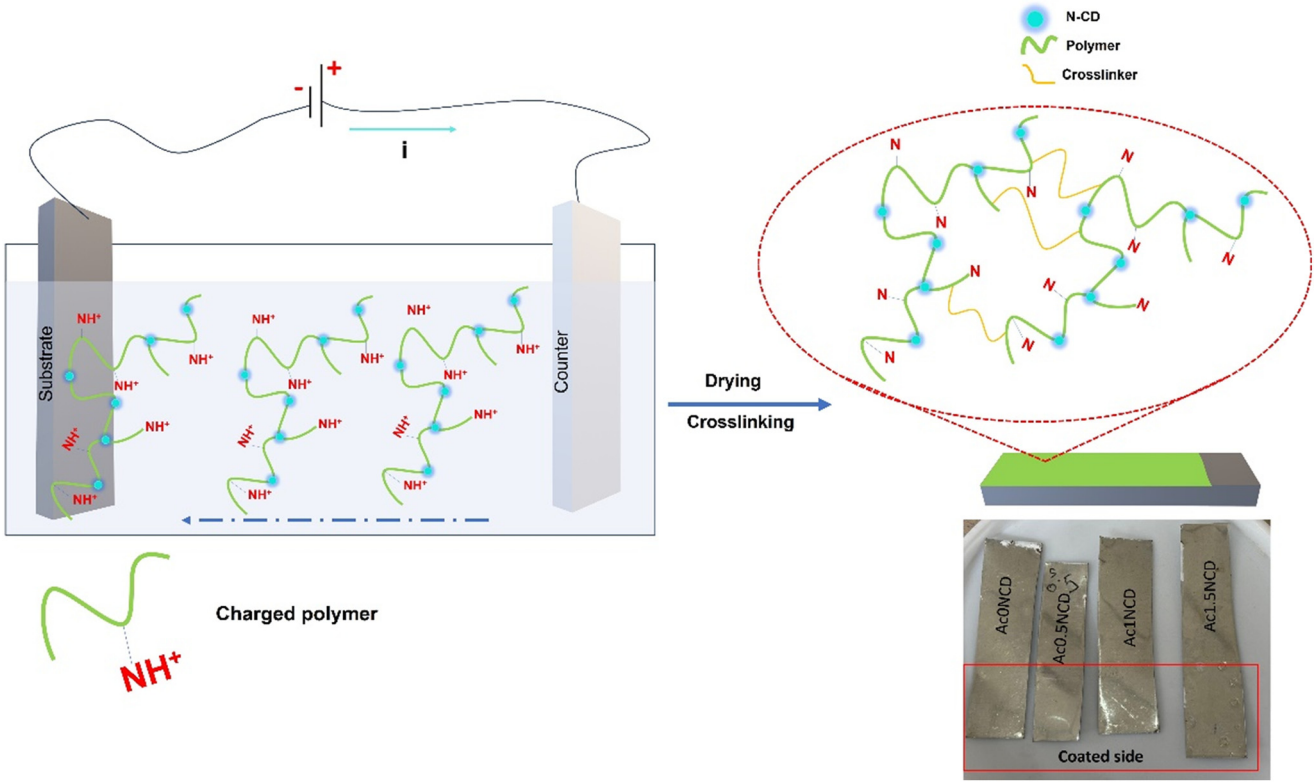

Fig. 2 Application and final appearance of the coating by cathodic electrodeposition (CED) and the photographs of the coated samples.

(TEM, FEI Tecnai G2 20 S-Twin), X-ray diffraction (XRD, Rigaku Ultima IV) and atomic force microscopy (AFM, Bruker's Dimension Icon) were used to understand the structure of the N-CDs. Fourier transform infrared spectroscopy (FTIR, UATR spectrum Two) and X-ray spectroscopy (XPS, UNI-SPECS UHV) techniques were used to understand the chemical structure and the composition of the N-CDs.

2.6.3. Characterization of the coating. The dry film thickness (DFT) of the coating was measured using a digital DFT meter (Elcometer 456) in accordance with the ASTM D7091-13 standard. Adhesion of the coating to the substrate was evaluated through cross-cut adhesion testing, following ASTM D3359. In this test, the surface of the coating was scratched, adhesive tape was applied, and after 120 seconds, the tape was rapidly removed at a 180° angle.

The hardness of the coated samples was assessed using pencil hardness testing according to ASTM D3363. The surface wettability of the coated samples was understood by means of the water contact angle measurement using a DSA25 apparatus (KRÜSS GmbH, Germany). A droplet of water of 5 μL was precisely dispensed onto the coating surface with a syringe, and the contact angle was measured. Photographs of the water droplets were recorded, and multiple measurements were taken for each sample to ensure accuracy.

The morphology of the coating was examined by field emission scanning electron microscopy (FE-SEM) using a MIRA3 TESCAN instrument (USA). Coated aluminum panels were sectioned into small pieces, gold-coated using an automated sputter coater (Quorum Mini Sputter Coater, SC7620, UK), and then imaged at different magnifications.

Atomic force microscopy (AFM) was performed using Bruker's Dimension Icon AFM (USA) to analyze surface topography and roughness. Coated samples were examined with a silicon nitride tip in ScanAssist mode, capturing real-time topography data. The AFM images were processed using NanoScope Analysis software.

Fluorescence spectroscopy was used to investigate the quenching behavior of N-CDs in the presence of Al^{3+} and other metal ions, while visual detection under UV light enabled qualitative analysis. Similar methods were employed to detect the quenching behavior at different immersion times for an Al panel in 3.5 wt% NaCl solution. This gave both a qualitative and quantitative idea of the detection of the corrosion process in Al by "turn on" and "turn off" mechanisms.

Electrochemical impedance spectroscopy (EIS) and potentiodynamic polarization tests were conducted in a 3.5% NaCl solution at room temperature to assess the corrosion protection performance of the coatings. A Voltalab 10 system (PGZ 100, Radiometer Analytical SAS, France) was used for the measurements, connected to a PC running VoltaMaster 4.0 software. The experiments were performed in a three-electrode cell with the coated sample as the working

electrode (WE), a platinum mesh as the counter electrode (CE), and an Ag|AgCl|KCl saturated reference electrode (RE). The working electrode was polished to expose a 0.6 cm^2 area. EIS measurements were taken with 10 mV amplitude over a frequency window of 1 MHz to 10 mHz, measured at the open circuit potential.

Potentiodynamic polarization was performed according to the ASTM G5 standard. Before testing, the samples were immersed in a 3.5% NaCl solution, and the open circuit potential was recorded. The polarization scan was conducted from −250 mV to +250 mV (*vs.* OCP), scanning at a rate of 0.5 mV s^{-1} in the anodic direction. Eqn (1) was employed to calculate the corrosion rates.

$$\text{Corrosion rate (mm per year)} = \frac{3.27 \times E_w \times i_{corr}}{D \times A} \quad (1)$$

where i_{corr} = corrosion current (mA); E_w = equivalent weight of Al = 9.0 g mol^{-1}; D = density of mild Al (2.9 g cm^{-3}); A = area of the dipped specimen (~1 cm^2).

3. Results and discussion

3.1. N-CD characteristics

3.1.1. Structural analysis. The structural and morphological characteristics of the nitrogen-doped carbon dots (N-CDs) were investigated *via* transmission electron microscopy (TEM), as shown in Fig. 3a. EM images illustrate well-dispersed N-CDs with an irregular morphology. The N-CDs appear amorphous and exhibit particle sizes in the range of 2–5 nm, consistent with prior reports.[21]

The crystalline nature of the N-CDs was further examined using X-ray diffraction (XRD), and the data are presented in Fig. 3b. The diffraction peak at 2θ = 22° corresponds to the (002) plane, indicative of the graphitic structure within the carbon dots. Notably, the interplanar spacing of approximately 0.394 nm exceeds that of pristine graphene (0.34 nm), confirming successful nitrogen doping. This doping leads to increased *d*-spacing, characteristic of amorphous carbon domains.[21]

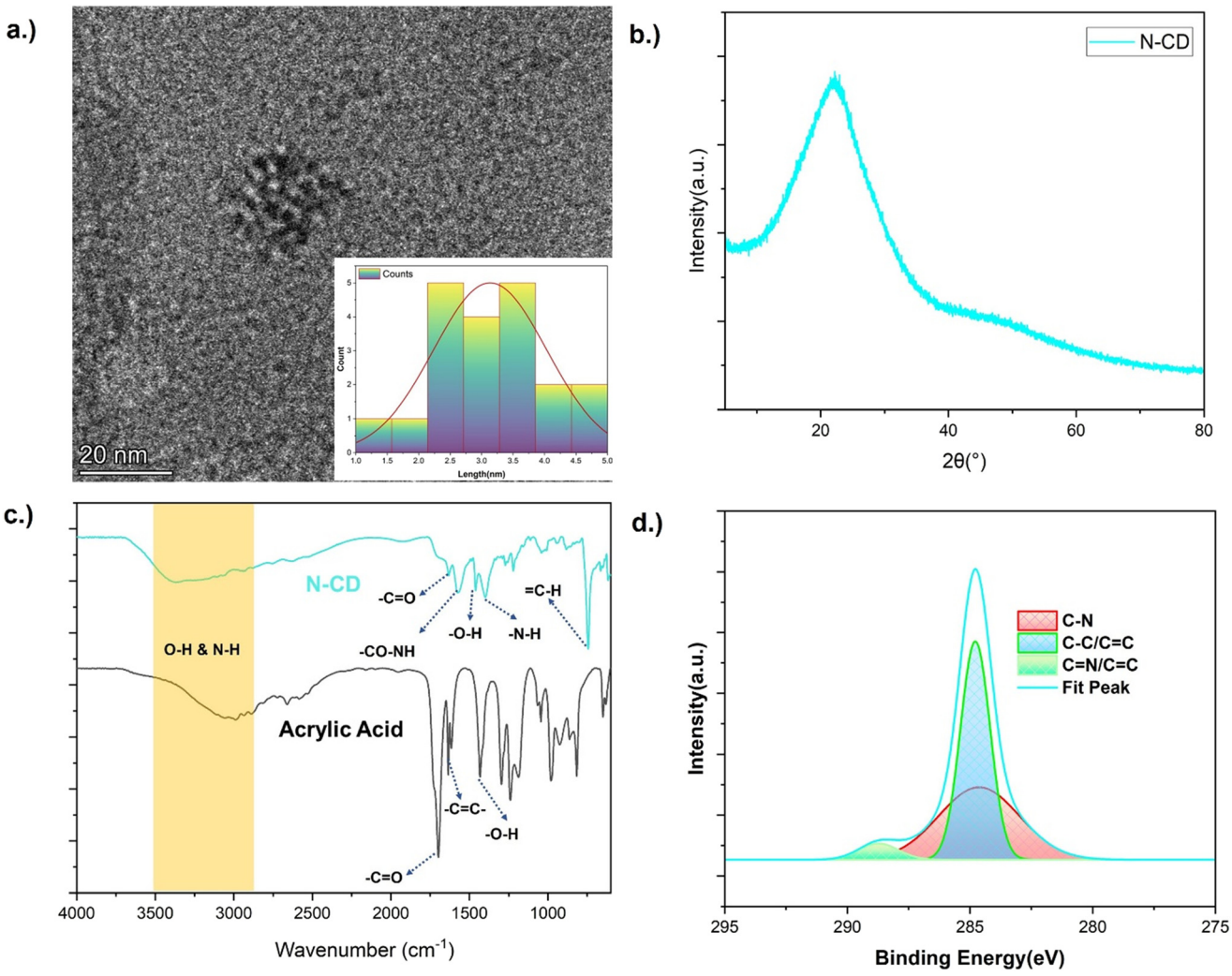

Fig. 3 Characterization of the synthesized N-CDs *via*: a.) TEM (size distribution of the N-CDs); b.) XRD; c.) FT-IR; d.) C 1s XPS spectra.

3.1.2. Spectroscopic analysis. Fig. 3c presents the FTIR spectra of the nitrogen-doped carbon dots (N-CDs) and acrylic acid. At 3380 cm^{-1}, the broad absorption peak corresponds to N–H groups, while the peak at 1627 cm^{-1} is attributed to C═O stretching vibrations.[21] The peaks at 1461 cm^{-1} and 1568 cm^{-1} are assigned to C–N (ref. 22) and N–H bonds,[23] respectively, confirming the presence of nitrogen-doped functional groups. The amide groups confirm the doping of nitrogen onto the carbon dots. The appearance of amide groups substantiates the successful nitrogen doping in the carbon dots. Additionally, the reduced intensity of the –C═C– peak at 1633 cm^{-1} in acrylic acid indicates polymerization of the carbon precursor during high-temperature synthesis. The peak at 742 cm^{-1} corresponds to the in-plane bending vibrations of aromatic C–H groups, originating from *para*-phenylenediamine precursors.[21]

The three elements C, N and O can be seen from the XPS spectra of the N-CDs confirming the doping of nitrogen on the carbon dots (Fig. S3a†). The C 1s XPS spectrum, shown in Fig. 3d, reveals a dominant peak at 284.6 eV, which is attributed to sp^2-hybridized carbon, consistent with the graphitic structure of the N-CDs.[22] A secondary peak at 285.2 eV corresponding to C–N bonds further confirms nitrogen doping.[24] The peak at 283.7 eV represents C–O and C═O bonds. The N 1s (Fig. S3b†) spectrum shows the pyridinic and the pyrrolic N and the deconvolution spectrum of O 1s (Fig. S3c†) displays 3 peaks assigned to C–O–H, C–O and C═O. These results obtained from the XPS are in agreement with the data obtained from FTIR, confirming the formation of N-CDs.

Together, the data from TEM, XRD, FTIR, and XPS confirm that the nitrogen-doped carbon dots have been synthesized successfully.

3.2. Nanocomposite characteristics

3.2.1. Structural analysis. The acrylic polymer, along with its constituent monomers, is depicted in Fig. 4a. The peak at 1750 cm^{-1} is indicative of the carbonyl group (C═O) in the acrylic segments. The stretching and bending vibrations of the C–O, C–C, and C–OH groups are observed between 1465 cm^{-1} and 1043 cm^{-1}. The enhancement of the peaks at 2800 cm^{-1} corresponds to the $-N(CH_3)_2$ vibrations,[25] confirming that the tertiary amine groups have been incorporated into the polymer to be utilized in neutralizing the polymer with an acid for cathodic electrodeposition. The disappearance of the peak between 1600 cm^{-1} and 1700 cm^{-1}, corresponding to the C═C double bond, confirms the occurrence of addition polymerization. The characteristic peaks of –OH, $-N(CH_3)_2$ and acrylic groups present in the synthesized resin confirm the successful formation of the acrylic polymer.

3.2.2. Thermal performance. The thermal performance of the coating formulations was evaluated by TGA up to a temperature of 600 °C. The DTG curves in Fig. 4b show that there is 3-stage degradation at 180 °C, 240 °C, and 370 °C as seen in the work of Harb *et al.*[11] This pattern of degradation is due to the high amount of MMA present as a monomer. Polymethylmethacrylate (PMMA) exhibits a similar trend of DTG curves[26] due to the cleavage in the linkages between consecutive acrylic monomers and then the vinyl terminated linkages. This is followed by the degradation of the main polymer chain. This copolymer undergoes similar degradation steps leading to a similar DTG curve.

The incorporation of the N-CDs in the nanocomposite does have some effect on its thermal stability as seen in Fig. 4b. As evident, the addition of N-CDs induces a marginal variation in the thermal stability of the coating, although the overall effect remains negligible. However, incorporation of 1 ml N-CDs in the nanocomposite increases the thermal stability to some extent. This mainly results from the enhanced interaction of the N-CDs and the matrix due to the –O═C–N–H– covalent bonds, followed by the hydrogen bonding between O and H and N and H, making the film much denser.[27]

3.3. Evaluation of the nanocomposites as coatings

3.3.1. Physical and mechanical characteristics. After complete curing, the coatings' mechanical and physical

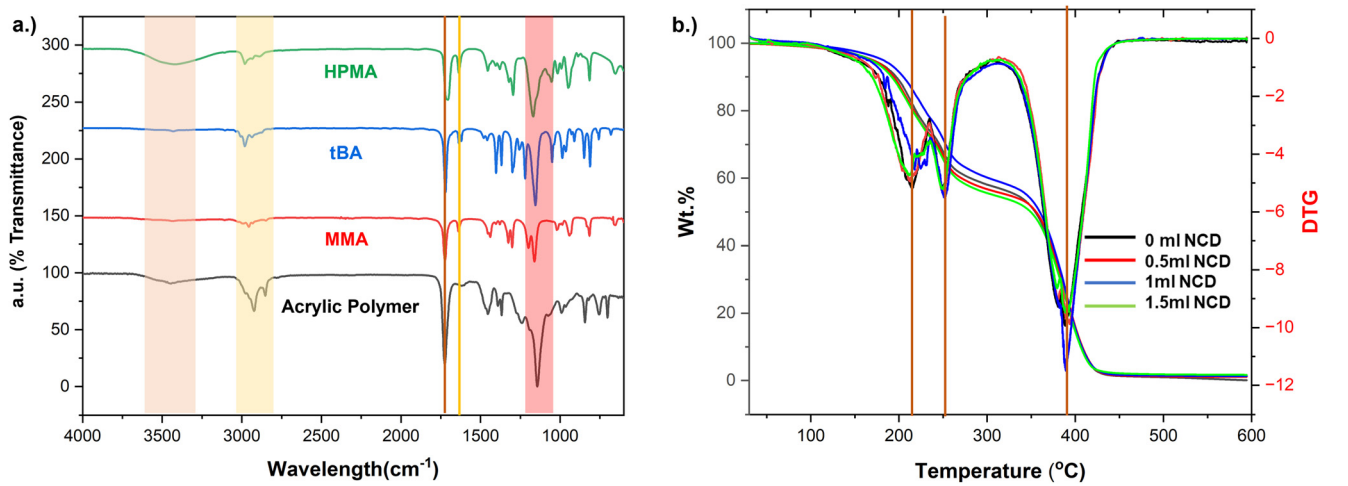

Fig. 4 a.) FTIR spectra of the monomers and the polymer; b.) thermal degradation data of the final coatings and DTG data of the final coatings.

properties were evaluated. All coated samples exhibited a smooth, glossy appearance. Visible defects such as pinholes or blisters were not observed in the Ac0NCD, Ac0.5NCD, and Ac1NCD coatings. However, as the N-CD concentration was increased in the Ac1.5NCD coating, blisters began to form, indicating that further increases in the N-CD content may compromise the coating integrity. Therefore, no additional experiments were conducted with higher N-CD concentrations.

The thickness of each coating was measured using a digital dry film thickness (DFT) meter. All the coatings were relatively thin, but a linear increase in thickness was observed as the N-CD concentration was elevated. This increase in thickness can be attributed to the tendency of N-CDs to form a denser layer on the substrate surface as well as the enhanced conductivity of the bath due to the addition of the N-CDs (as shown in Table S1 in the ESI†), enhancing the overall coating structure.[22] Further the deposition times were varied to obtain coatings with similar thickness to Ac1.5NCD in order to check the exact effect of the thickness on the coatings.

Cross-cut adhesion, pencil hardness, and flexibility tests were employed to determine the mechanical properties. According to the ASTM D3359, the adhesion of the coating to the substrates was tested by the cross-cut adhesion test.[28] The Ac0NCD coating exhibited a 4B rating whereas those with the N-CDs included exhibited a better adhesion of 5B, which is the best adhesion rating. The formation of the passivation layer on the substrate surface led to the better adhesion of the coating with the substrate.[22] The visual inspection of the coatings post the cross-cut adhesion test is shown in the ESI† (Fig. S6), where minimal flaking and clean edges further confirm the superior adhesion performance of the N-CD-modified coatings.

A pencil hardness of 5H was exhibited by the Ac0NCD coating. The surface hardness was mainly due to the presence of MMA segments in the copolymer. The incorporation of N-CDs increased the hardness of the AC0.5NCD, Ac1NCD, and Ac1.5NCD coatings to 6H. The –O═C–N–H– covalent bonds, which cause the matrix and N-CDs to interact more, and the hydrogen bonding between O and H and N and H, which causes the film to become considerably denser, result in the increased hardness of the coatings.

The flexibility of the coatings was evaluated using a conical mandrel. The coatings were found to be very flexible even after the incorporation of the N-CDs. The presence of the long chain *tert*-butyl acrylate caused the coatings to be flexible.

The thickness variation did not affect the mechanical properties of the coatings to any notable extent.

All the physical and mechanical properties are listed below in Table 2.

3.3.2. Hydrophobicity estimation *via* water contact angle measurement. Fig. 5a exhibits the contact angle of the coatings, while Fig. 5b illustrates the Cassie–Baxter effect and the enhanced surface roughness induced by N-CDs, which collectively contribute to the increased hydrophobicity of the coatings. The Al substrate coated with Ac0NCD, due to its excellent adhesion to the substrate because of the electrodeposition method, exhibited a relatively higher contact angle of 73.8° as compared to brush or dip-coated acrylics.[29] With the increase in the amount of N-CDs in the coating composition, the pendant –OH groups of the acrylic resin are hydrogen bonded with the N-CDs, reducing the interaction with water droplets coming to the surface and making the coating less hydrophilic.[11] The incorporation of N-CDs in the coating also enhances the interaction of the matrix with the substrate as well as with itself, making it less porous and thus resulting in less interaction with water molecules. Also, the presence of the N-CDs in the coating formulation increases the roughness of the coatings at a nano-level. This introduction of heterogeneity in the surface leads to the increase in the hydrophobicity of the coatings, as explained by the modified Cassie–Baxter model.[30] However, upon increasing the amount of N-CDs in the coatings, the surface is blistered and this leads to a massive decrease in the hydrophobicity of the coatings.

3.3.3. Morphological and topographical aspects of the coating. The morphology of the applied coatings was studied by SEM. The images obtained from SEM show that for the Ac0NCD coating, there are pores on the surface (Fig. 6a) mainly because of the evaporation of water from the surface during the drying process. However, the defects are less due to electrodeposition as compared to other coating methods like bar coating.[22] The role of N-CDs as nano-fillers is confirmed as the pores and other defects disappeared as they were filled up by the N-CDs (Fig. 6b). With increasing N-CD content, the roughness of the coatings enhances as seen in Fig. 6c. This makes the coatings more hydrophobic and is consistent with the water contact angle observations in

Table 2 Mechanical and physical properties of the coatings

Sample	Ac0NCD	Ac0.5NCD	Ac1NCD	Ac1.5NCD	Ac1.5NCD (15 s)	Ac1.5NCD (20 s)
Thickness (μm)	10	12	13	18	12	15
Texture	Smooth	Smooth	Smooth	Blistering on the surface	Blistering on the surface	Blistering on the surface
Cross-cut adhesion	4B	5B	5B	5B	5B	5B
Hardness	5H	6H	6H	6H	6H	6H
Flexibility	Good	Good	Good	Good	Good	Good

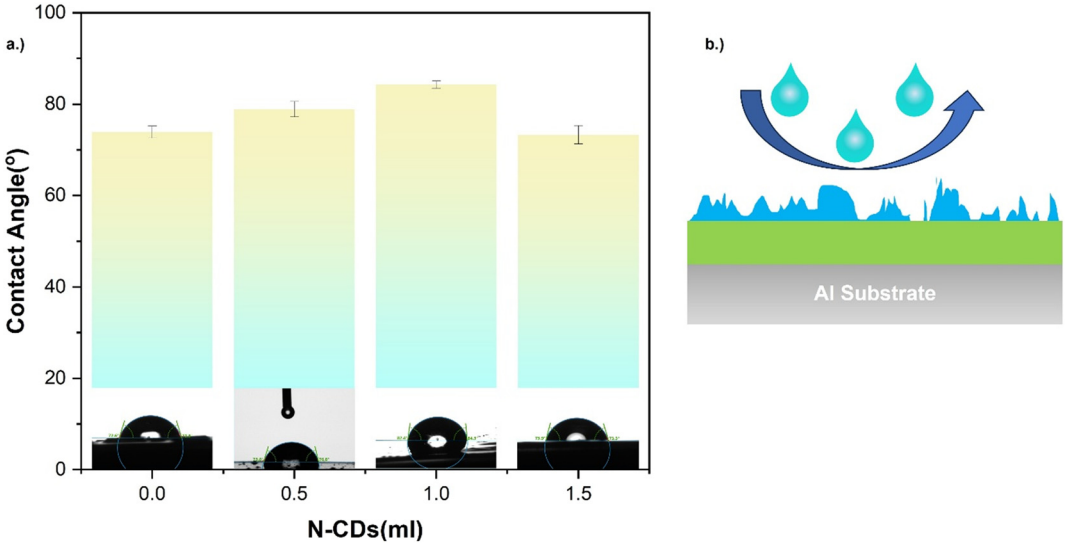

Fig. 5 Representation of: a.) the contact angle of the coatings with their photographs; b.) the Cassie–Baxter effect and enhanced roughness of the coating enhancing the hydrophobicity of the coatings.

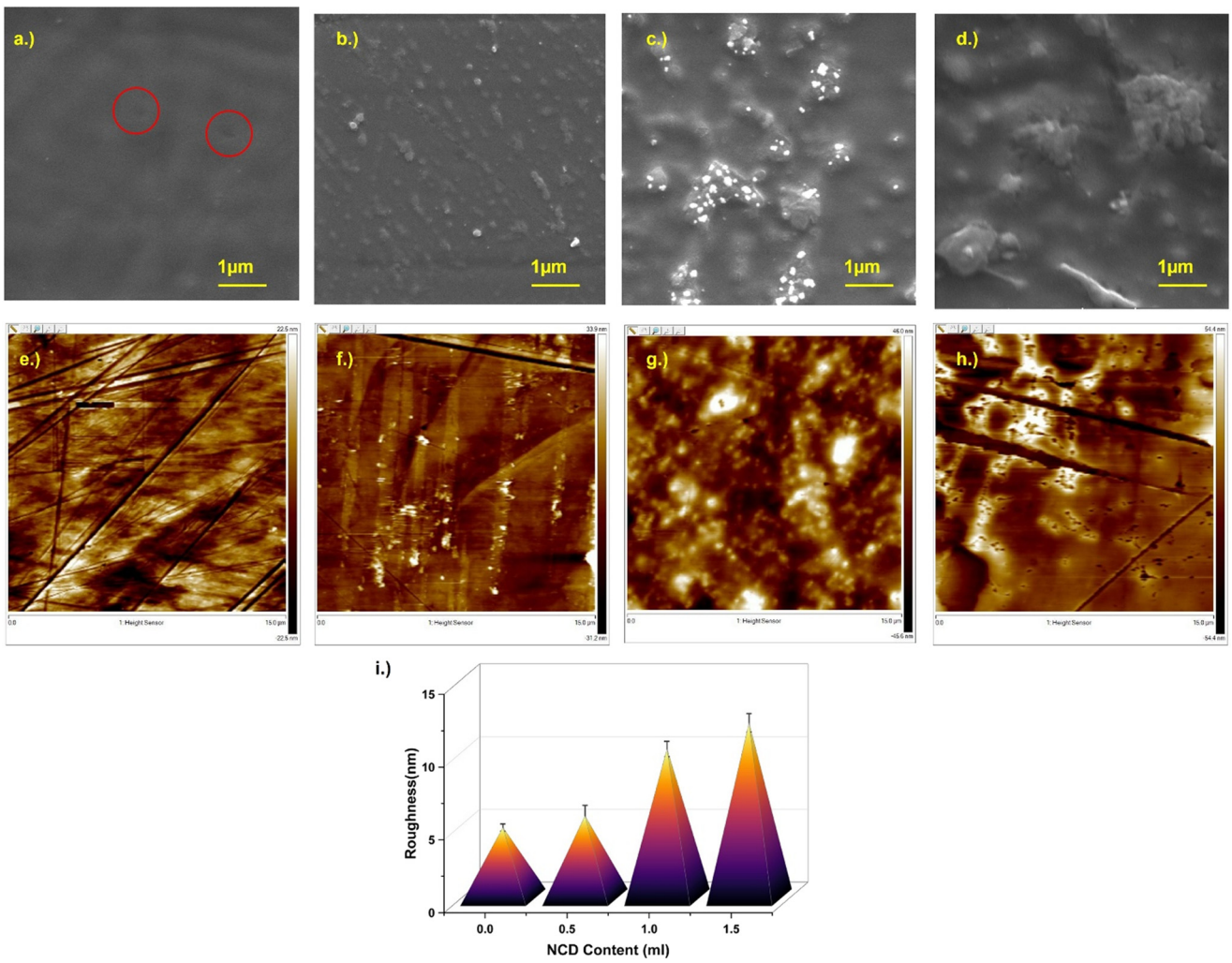

Fig. 6 SEM images of: a.) Ac0NCD, b.) Ac0.5NCD, c.) Ac1NCD, and d.) Ac1.5NCD; 2D AFM images of: e.) Ac0NCD, f.) Ac0.5NCD, g.) Ac1NCD, and h.) Ac1.5NCD; i.) roughness of the coatings.

section 3.3.2. A higher percentage of N-CDs leads to blistering of the coatings as seen in Fig. 6d. This can occur if the filler exceeds the optimum level and the filler–matrix interaction is replaced by filler–filler interactions.[31] Thus, from the SEM data we can conclude that the N-CDs act as nanofillers in filling up the pure polymer coating defects as well as enhance the roughness of the coatings making them more hydrophobic, if used in optimum dosage.

The topology of the resin-coated Al panels was examined by AFM analysis (Fig. 6e–h). In section 3.3.2, it was described that the Cassie–Baxter effect and the development of peak and valley-like structures on the surface increase the hydrophobicity of the coatings. The surface roughness (R_a) of the coated samples was analyzed using NanoScope Software. It is seen that with the increase in the N-CDs, there is development of peak and valley-like structures which result in the increase in the R_a values of the coatings from 4.8 μm to 12.0 μm (Fig. 6i). Thus, it can be confirmed that due to the increased roughness of the coatings, there is an increase in the hydrophobicity of the coatings and the results are consistent with the observations made with water contact angle measurements.

3.4. Performance of the coating

3.4.1. Performance in chemical environments. The chemical properties of the coatings were assessed through immersion tests in acidic, neutral, and alkaline environments to evaluate their resistance under various conditions. Upon 24 hour immersion in deionized (DI) water and a 5% HCl solution, the coatings demonstrated excellent resistance. This strong performance is attributed to the highly crosslinked structure formed between the –NCO groups of the Cyamel crosslinker and the –OH groups of the resins. The inclusion of N-CDs further contributed by enhancing the coating adhesion to the substrates and promoting the deposition of a stable adherent layer.

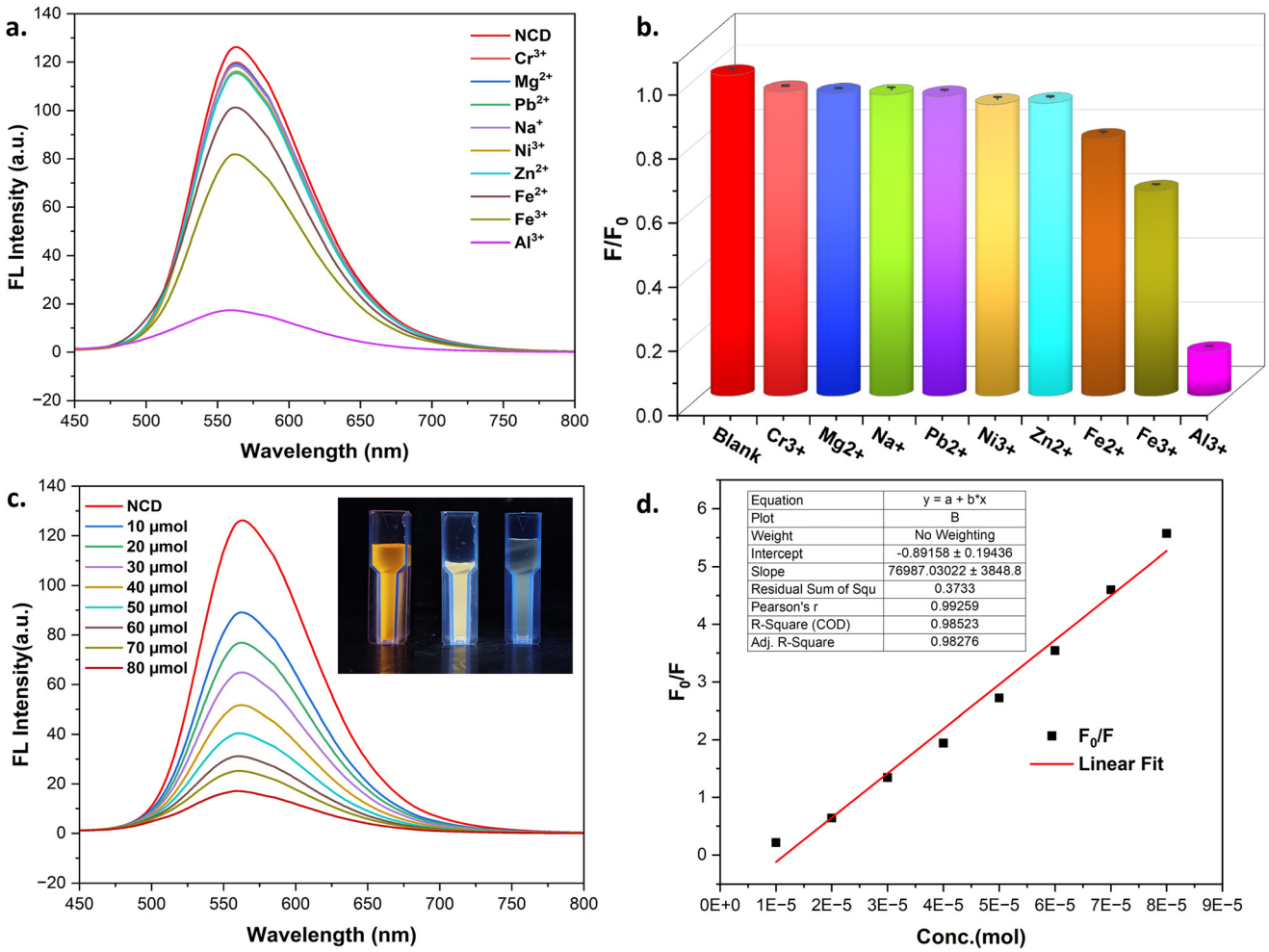

Fig. 7 a.) Quenching behavior of the N-CDs at 560 nm with different metals, confirming the selective quenching with Al^{3+}; b.) the ratio of the fluorescence intensity of N-CDs at 560 nm (F/F_0) after and before the addition of Al^{3+} and other metal ions; c.) the quenching behavior of the N-CDs with Al^{3+} ions at different concentrations (inset showing the decreasing intensity of the N-CDs with increasing Al^{3+} ion concentration); d.) linear fitting of the ratio of fluorescence intensity at 560 nm *versus* the concentration of Al^{3+} (10–80 μmol).

However, under 36 hour immersion in a 5% NaOH solution, the coatings exhibited reduced resistance. For the Ac0NCD and Ac1.5NCD coatings, delamination occurred post-immersion, while the Ac0.5NCD and Ac1NCD coatings experienced significant gloss reduction and the appearance of brown spots.

Solvent resistance was examined using solvent-rub tests. In the non-polar xylene rub test, 150 cycles caused no observable degradation. In contrast, in the polar methyl ether ketone (MEK) rub test, 100 cycles resulted in a noticeable gloss reduction, likely due to the interaction between the polar resins and the polar MEK solvent.

Furthermore, the coated samples were immersed in ethanol for 24 h, and weight changes were recorded pre- and post-immersion. The results showed a 95.8% crosslink content, indicating almost complete crosslinking of the coatings.

3.4.2. Investigation of the N-CDs in Al^{3+} sensing. The yellow-emitting N-CDs exhibited a characteristic emission band in the fluorescence spectra at 560 nm as seen in Fig. 7a. The fluorescence intensity at 560 nm was quenched with the increase in Al^{3+} and the quenching progressively increased with increasing Al^{3+} concentration. In the plot of the fluorescence quenching ratio of the N-CDs and Al^{3+} (as seen in Fig. 7b), it was found that the N-CDs can respond very readily to Al^{3+} in a wide range of concentrations (10–80 μmol). As seen from the inset of Fig. 7c, the color gradually faded and it finally disappeared with increasing concentration of Al^{3+} under UV light, suggesting very easy detection by the naked eye. Also, the quenching ratio varied linearly with the concentration of Al^{3+} in the range of 10–80 μmol, from where the LOD (limit of detection) was determined[32] to be 72 μmol. As confirmed from the XPS and FTIR analysis, the surface of the prepared N-CDs is mainly composed of functional groups such as –OH, –COOH, $–NH_2$, and –C═O. These active organic groups readily interact with Al^{3+}, forming Al^{3+}–NCD complexes. Consequently, electron transfer occurs, resulting in the fluorescence quenching of N-CDs.[33–35] Thus, detection of Al^{3+} using the dual-mode visual observation and fluorescence spectroscopy enables qualitative and quantitative analysis. This approach offers a valuable opportunity for real-time and visual monitoring of aluminium corrosion.

3.4.3. Real-time detection and monitoring of Al corrosion. As is widely known, the biggest limitation to metals is their susceptibility to corrosion. Al plates were immersed in 3.5 wt% NaCl solution and exposed for corrosion. The weight

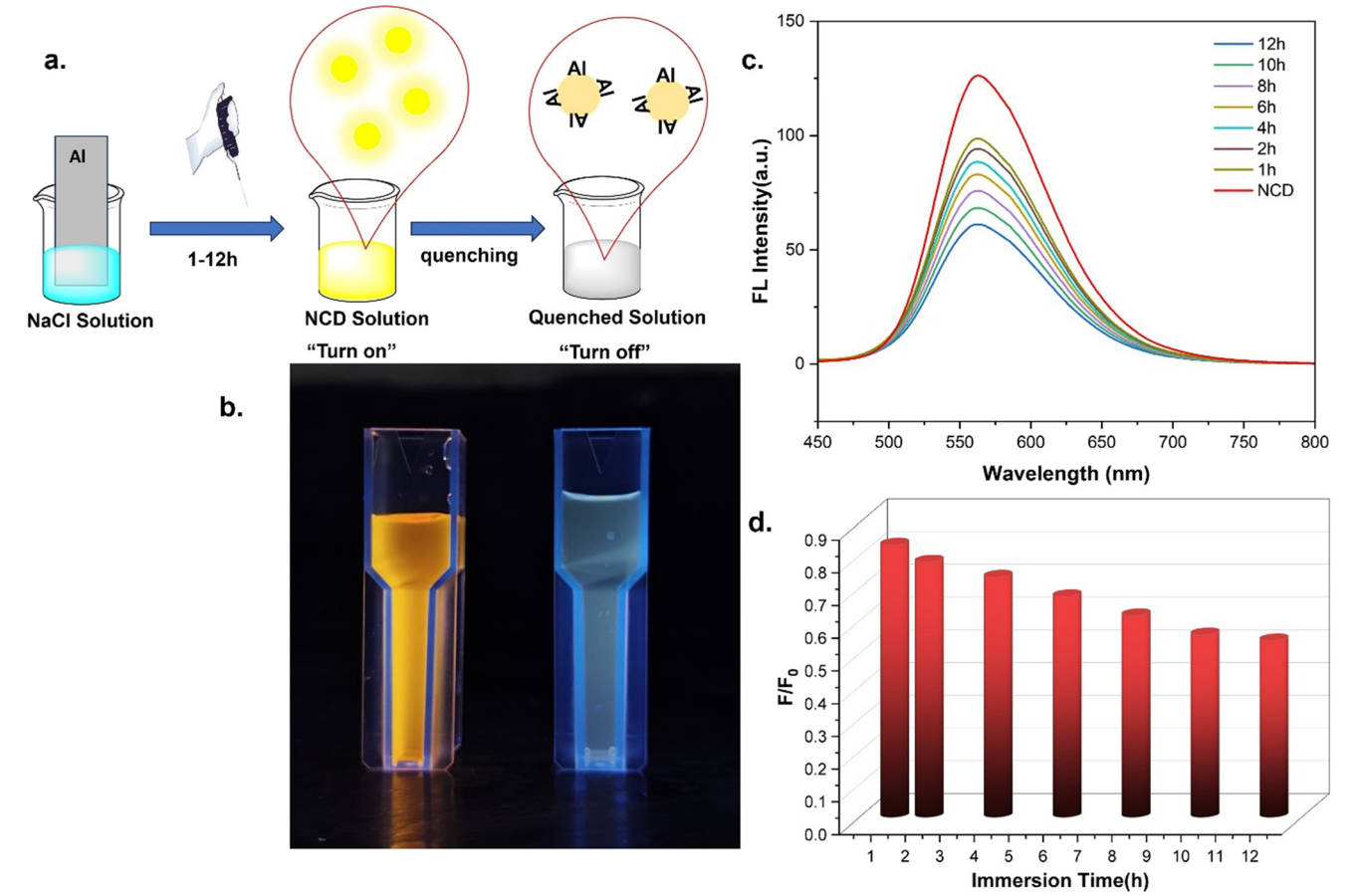

Fig. 8 a.) Process and mechanism for the immersion time-quenching study; b.) digital photographs of the "turn on" and "turn off" mechanisms in the detection of corrosion initiation; c.) quenching behavior of the N-CDs at 560 nm at different immersion times; d.) the ratio of the fluorescence intensity of N-CDs at 560 nm (F/F_0) at different immersion times.

loss was calculated to be 320.5 mg m^{-2} h^{-1} after 12 h, confirming the dissolution of the Al substrates in the solution, in the form of Al^{3+} and $Al(OH)_3$. Thus, Al^{3+} can work as the indicator for the degree of corrosion. The increasing immersion time results in the increased concentration of Al^{3+} in the NaCl solution, confirming the increasing corrosion degree. The solution is added to the N-CD solution, and the fluorescence of the N-CDs is quenched (Fig. 8c). The changes in the intensity of the fluorescence and the degree of corrosion can be determined. The excellent quenching of the N-CDs by the "turn-off" phenomenon can be monitored using a fluorescence spectrometer as well as the naked eye (Fig. 8b). Thus, it can be confirmed that the N-CDs can be effectively utilized in the detection of corrosion in the Al substrates. However, not only the detection, but also the inhibition of the corrosion of Al was also tested by electrodepositing the carbon dots with acrylic resins on the aluminium substrates.

3.4.4. Performance in a corrosive environment. The coatings' performance in providing corrosion protection was assessed using EIS, presented in the Nyquist plots. The interaction between the substrate, coating, and electrolyte is typically represented by a set of resistances and capacitances, connected in series and parallel, as illustrated in Fig. 9c. The equivalent circuit (Fig. 9c) employed to model the Nyquist plot consists of a solution resistance (R_s) between the reference and working electrodes, along with two resistances (R_p and R_c) connected in parallel with two constant phase elements (CPE_1 and CPE_2). R_p corresponds to the resistance of the outer coating layer, while R_c reflects the resistance of the inner layer. As the outer coating becomes more compact and less porous, the R_p and R_c increase. All the current components are tabulated in Table S3 in the ESI.† The CPEs describe the dielectric behavior of the electrolyte–coating interface, with higher CPE values indicating improved barrier properties, as greater dielectric strength enhances the insulating characteristics of the CPEs. If the polymer coating is compromised, the dielectric strength diminishes considerably, reducing the overall impedance. The Nyquist plot provides insights into both the capacitance and resistance of the coatings.

Fig. 9a and a′ exhibit the Nyquist plots of the coatings. The bare Al substrate has an impedance of around 2 kΩ. The application of the bare polymer coating (Ac0NCD) alone

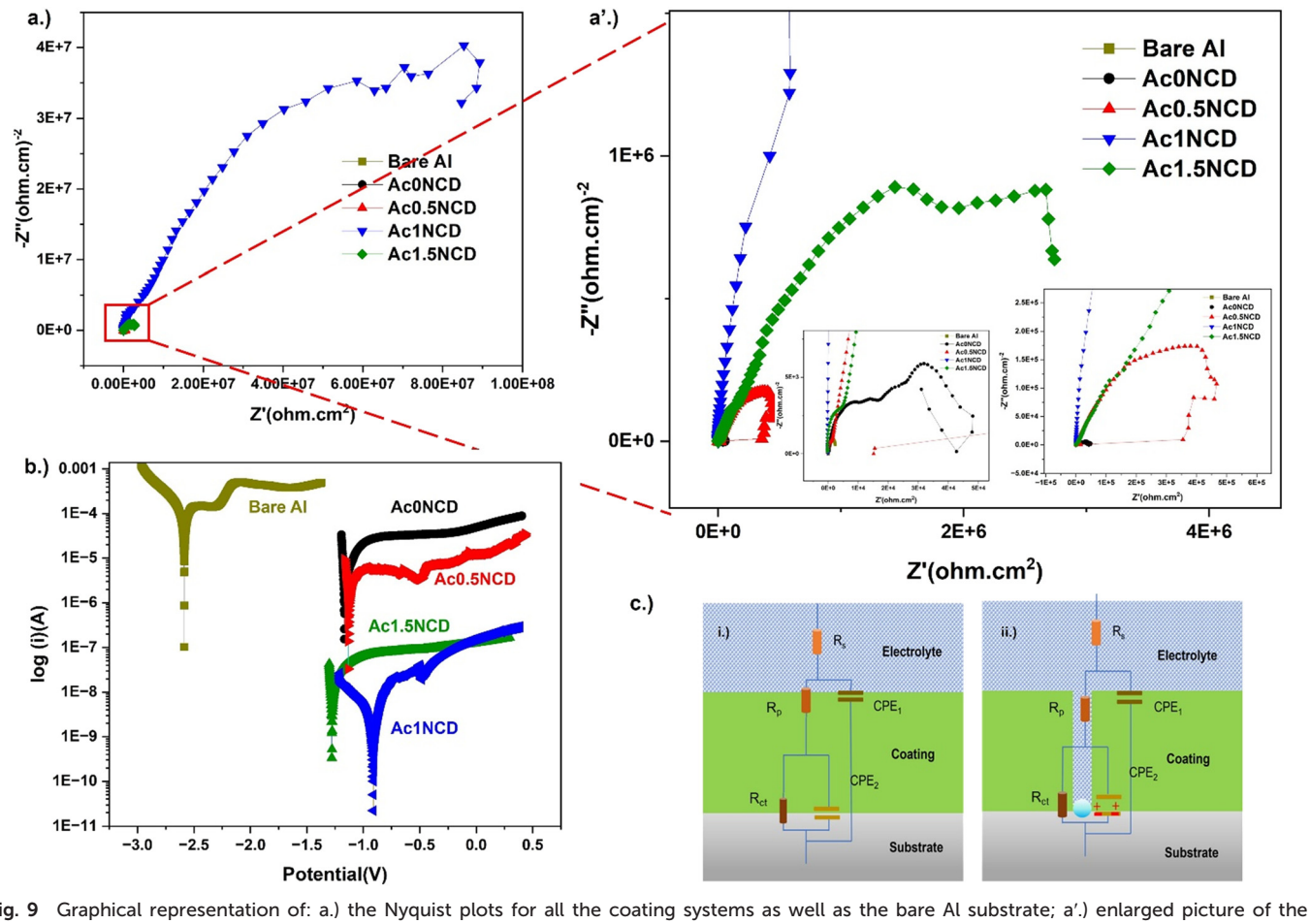

Fig. 9 Graphical representation of: a.) the Nyquist plots for all the coating systems as well as the bare Al substrate; a′.) enlarged picture of the Nyquist plot; insets showing further enlarged versions for better representation; b.) Tafel curves of all the coating systems as well as the bare Al substrate; c.) the equivalent circuit representation of a coated substrate: i.) in its intact form; ii.) due to coating defects like water uptake and electrolyte ingress.

enhances the corrosion inhibition with an increased impedance of around 6.5 kΩ. The incorporation of the N-CDs into the coating composition enhances the corrosion inhibition properties of the coating. Addition of 0.5 ml of N-CD increases the anti-corrosive property of the coating. A further massive increase is seen in the impedance of the coating to a staggering range of 10^4 kΩ. The multiple factors of the N-CDs filling the pores and defects in the coating enhanced the interaction between the N-CDs, forming a passive layer on the metal surface, and the increase in the hydrophobicity enhances the anti-corrosive properties of the N-CD loaded coatings. However, due to the blistering in Ac1.5NCD, the impedance of the coating drops, signaling a decrease in the properties. The calculated charge transfer as well as the solution resistance also shows similar properties (Fig. S2†). The changes in the impedance values (5.8×10^5 Ω and 1×10^6 Ω) due to the varying thickness and the varying deposition time (15 s and 20 s respectively) for the Ac1.5NCD coating had a limited effect as compared to the increase due to the introduction of the N-CDs. Thus, it can be confirmed that N-CDs are very effective in enhancing the anti-corrosive properties of the cathodically deposited coatings which are quite high compared to those reported in the literature for other nanoparticles like TiO_2, ZnO and silica[13,36–39] (Fig. S5†), but a higher dosage of N-CDs will lead to degradation of the properties.

3.4.5. Estimation of the rate of corrosion. Tafel curves, derived from potentiodynamic potential measurements as shown in Fig. 9b, are used to estimate the corrosion current (i_{corr}). Due to the absence of well-defined linear Tafel regions in the polarization curves of coated samples, corrosion current densities (i_{corr}) were estimated by drawing tangents to the anodic and cathodic branches, with their intersection taken as the i_{corr} value. This approach, while empirical, is widely used for high-performance coatings where classical Butler–Volmer behavior is not observed. By analyzing these curves, the corrosion current density can be determined, which allows for an estimation of the coating's lifetime. It can be seen that with the increase in the N-CD content in the coating, the i_{corr} is increased manifold from 10^{-5} A in the case of the Ac0NCD to a staggering 10^{-9} A in the case of Ac1NCD. The E_{corr} (potential where corrosion occurs) also increases with the NCD content, indicating that the initiation of the corrosion is also slow and a higher potential is required for the materials to corrode. As seen in section 3.4.3, the blistering results in the decrease in the corrosion current and the corrosion potential as the electrolytes can penetrate through the defects in Ac1.5NCD. As a result, the i_{corr} is reduced as compared to Ac1NCD, indicating a faster corrosion rate. Similar trends have been confirmed from the coated systems' open circuit potential (OCP) values (Fig. S1†). Also, the E_{corr} is reduced indicating the ease of the electrolytes to penetrate through the coating onto the substrate. Thus, it can be concluded successfully that Ac1NCD is the most optimized system which leads to the formation of the passive layer, and the enhanced matrix–nanofiller interaction results in the higher corrosion inhibition of the NCD-loaded coating systems. Only one equivalent circuit model, as shown in Fig. 9c, was used throughout for all the coatings. Changes in the electrochemical behavior are reflected by variations in the fitted values of the resistive and capacitive elements (R_p, R_c, CPE_1, and CPE_2) over time, rather than a shift in the circuit topology. This approach is in alignment with earlier studies such as by Harb *et al.*,[40] where a similar dual time constant circuit was applied, and the temporal evolution of elements was used to monitor coating degradation processes.

The enhanced corrosion protection due to the application of the coating and the addition of N-CDs is tabulated in Table 3.

The EIS spectra were fitted using a two-time-constant equivalent circuit model consisting of solution resistance (R_s), coating resistance (R_p), and charge transfer resistance (R_{ct}), each in parallel with a constant phase element (CPE). The fitted CPE parameters were used to derive the coating capacitance values (C_1 and C_2), which represent the dielectric behavior of the outer and inner coating layers, respectively. These capacitance values are summarized in Table S2 (ESI†), while the resistance values are depicted in Fig. S3.†

3.5. Real-time performance evaluation by the immersion test

In order to simulate localized corrosion behavior, all the samples, including bare metal, were inscribed prior to immersion, enabling consistent evaluation of corrosion propagation from a defined defect. While not standard for bare substrates, this approach provided a control reference for visual comparison. The test procedure and analysis follow the ASTM D1654 guideline, which addresses underfilm corrosion behavior in inscribed specimens.[41,42] Fig. 10 displays images of the coated and uncoated samples. The uncoated aluminum panels exhibited extensive corrosion within 30 days. In contrast, substrates coated with the acrylic-based coatings demonstrated significant resistance to corrosion for the same duration. While the acrylic coating without N-CDs (Ac0NCD) displayed degradation in the subsequent month, the incorporation of N-CDs effectively suppressed the corrosion process.

Notably, the Ac0.5NCD coating began to show signs of degradation after 30 days, whereas the Ac1NCD and Ac1.5NCD coatings remained unaffected for 60 days. Although localized corrosion was observed around the blisters in the Ac1.5NCD coating, the unaffected areas

Table 3 Corrosion resistance and the rate of corrosion data for all the coatings

Coating	Z (Ω)	i_{corr} (A)	Corrosion rate (mm per year)
Ac0NCD	6.5×10^3	6.1×10^{-5}	6.1×10^{-4}
Ac0.5NCD	4.8×10^4	1.9×10^{-5}	2.0×10^{-4}
Ac1NCD	7.2×10^7	8.5×10^{-8}	8.5×10^{-7}
Ac1.5NCD	1.6×10^6	6.7×10^{-7}	6.7×10^{-6}

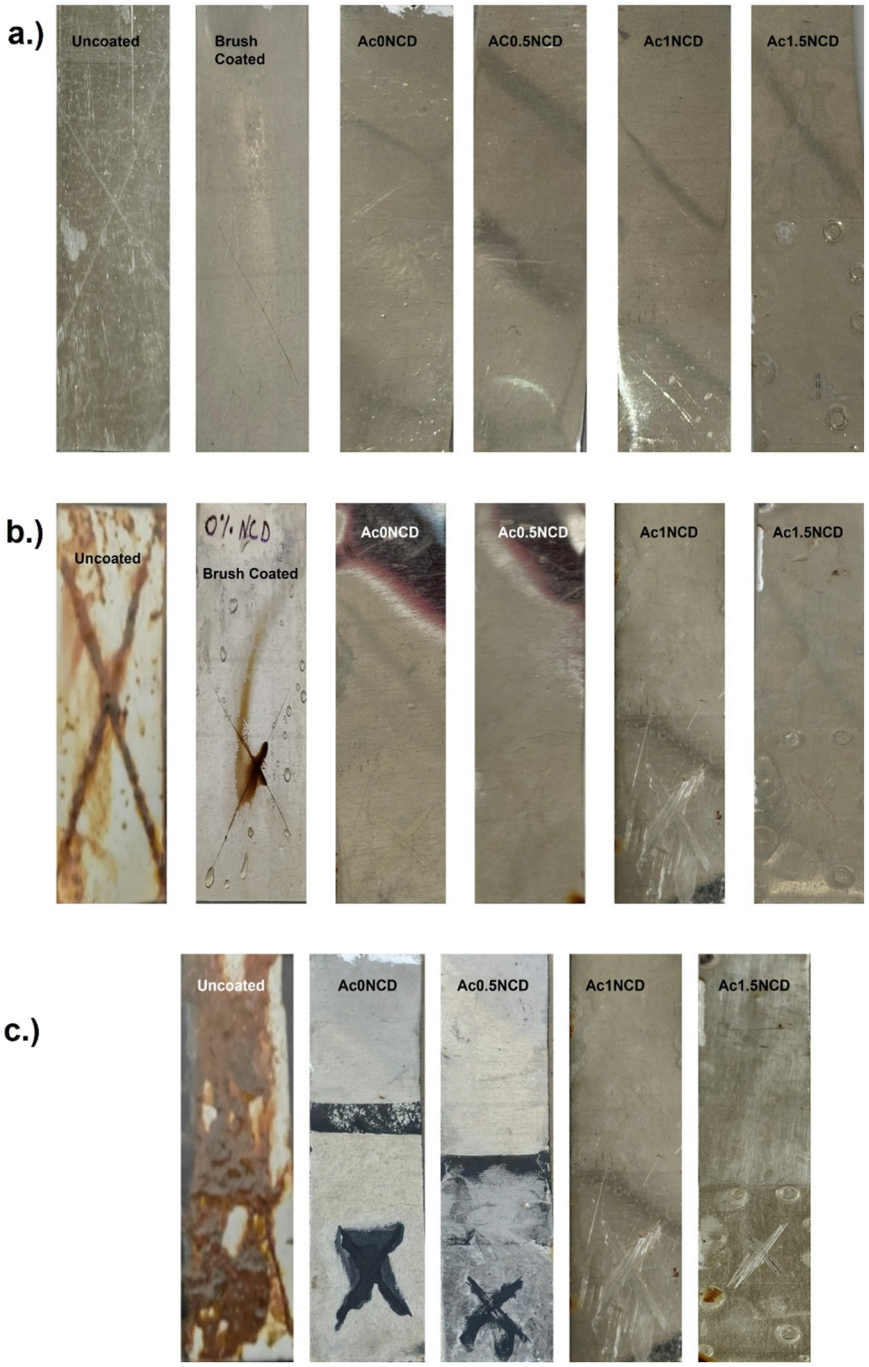

Fig. 10 Digital photographs of the immersion tested panels after a.) 0 days, b.) 30 days and c.) 60 days.

remained intact, highlighting the superior corrosion resistance imparted by N-CDs. These findings confirm that the inclusion of N-CDs in cathodically deposited acrylic coatings significantly extends substrate durability.

For comparison, the Ac0NCD resin was also applied *via* brush coating and subjected to similar testing over a 30-day period. As shown in Fig. 10b, the cathodically deposited coatings outperformed the brush-coated samples in terms of corrosion resistance. This demonstrates the superior efficacy of the cathodic electrodeposition (CED) technique over traditional application methods, underscoring its potential for enhanced protective performance.

In addition to electrochemical measurements, the early-stage corrosion detection capability of the coatings was evaluated through their fluorescence quenching behavior under UV light. As shown in ESI† Fig. S4, the fluorescence intensity visibly decreased in areas where Al^{3+} ions leached from the substrate, effectively indicating localized corrosion onset. This quenching mechanism highlights the smart-sensing capability of the coating system, offering a visual and

non-invasive means of identifying early corrosion activity prior to visible degradation.

3.6. Mechanism of corrosion resistance

The corrosion inhibition properties of N-CDs arise from a combination of synergistic factors, as illustrated in Fig. 11. The primary mechanism is the enhanced interaction between the N-CDs and the acrylic matrix, facilitated by the formation of covalent –O═C–N–H– bonds and hydrogen bonding between O–H and N–H groups. These interactions contribute to a denser film structure.[27] Additionally, the nanoscale dimensions of the N-CDs allow them to function as nano-fillers, effectively filling voids formed in the coating due to solvent evaporation during the drying process.[43] Upon contact with the aluminium substrate, the N-CDs form a dense passivation layer *via* physical adsorption and chemisorption mechanisms.[22] This passivation layer acts as a robust barrier, impeding the diffusion of electrolytes to the substrate surface and thereby significantly mitigating the rate of corrosion.

Furthermore, N-CD incorporation increases the surface roughness of the coating, leading to increased hydrophobicity through the Cassie–Baxter effect. This enhanced hydrophobicity reduces the residence time of corrosive species on the coated surface, further improving the anticorrosive performance of the acrylic coatings. Collectively, these factors establish N-CDs as highly effective corrosion-inhibiting agents in cathodically deposited coatings.

3.7. Practical implication of the turn-off mechanism

The demonstration of the quenching behavior of the N-CDs in the presence of Al^{3+} and especially in the corrosion solution, *i.e.*, after the initiation of the corrosion process of Al in a salt solution, can be exploited to detect the initiation as well as the progression of the corrosion of Al. We propose the design of a corrosion monitoring device which works in a similar way to pH paper. We demonstrate the same in a very easy-to-make device where we used N-CD solution as an ink to write the words "NO CORROSION" on 18 GSM paper. The words are visible under fluorescent light. The words remained intact when dipped in normal water or salt solution. However, when the paper was dipped in the corrosion solution of the Al panel, we observed that the part dipped in the solvent, *i.e.*, the "NO" was quenched by the Al^{3+} ions present in the solution, confirming the corrosion of the sample. Thus, it is seen that when the paper was dipped in water or any other solution, the "NO CORROSION" written on the paper was quite clearly visible. When the paper was dipped in the corrosion solution of Al, it read only "CORROSION" under UV light (Fig. 12a), confirming the advent of the corrosion of the dipped aluminium panel.

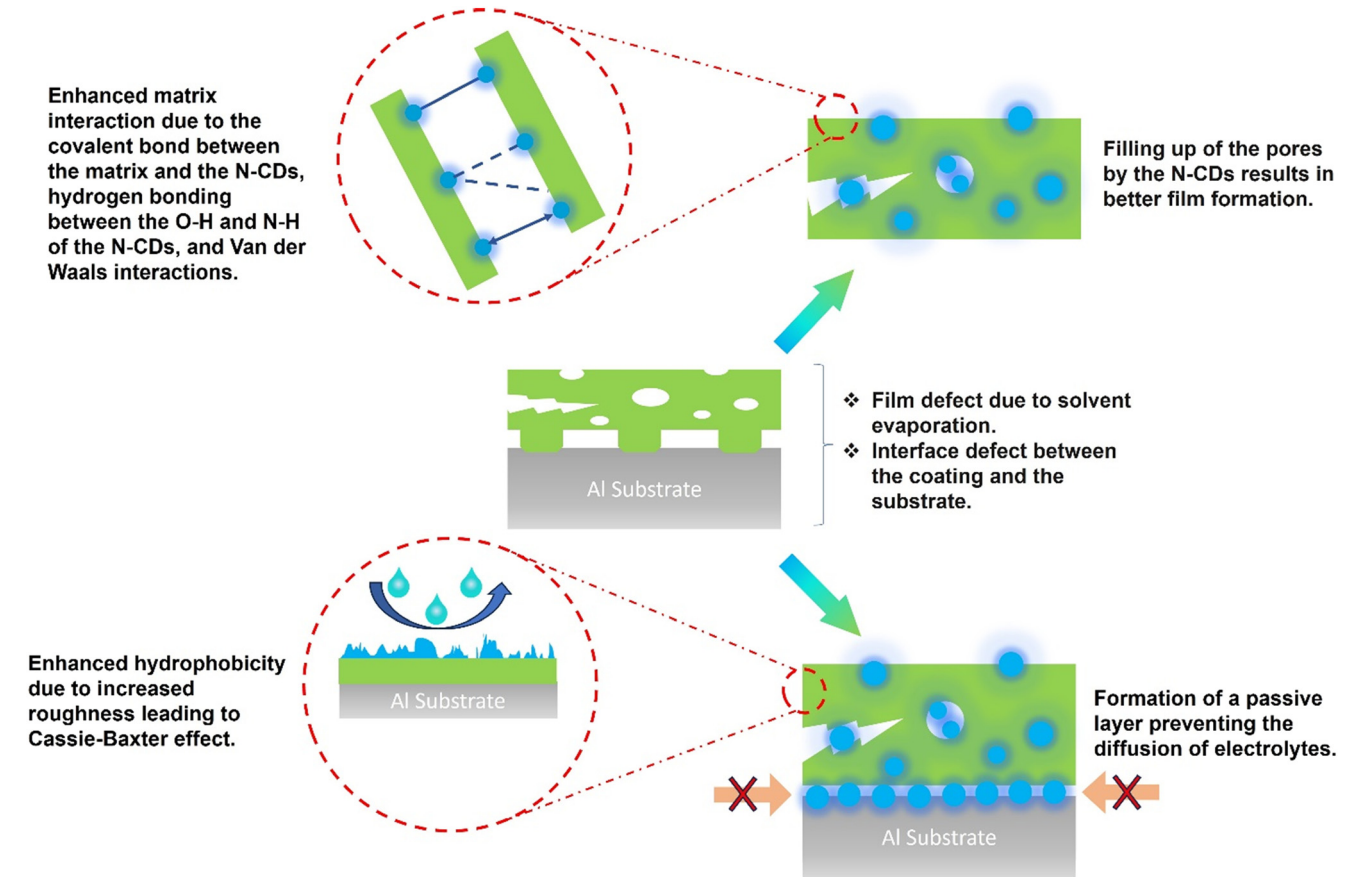

Fig. 11 The corrosion inhibition mechanisms at play in favor of the N-CD-CED composite coating.

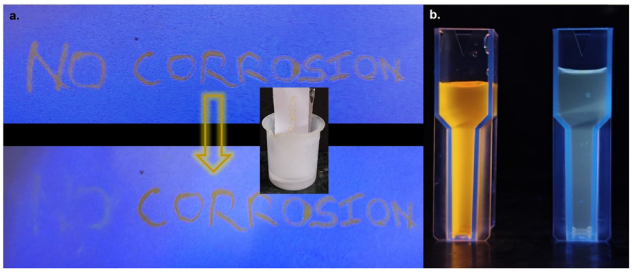

Fig. 12 a.) Design and application of the "turn off" mechanism of N-CDs for the development of a pH-paper like material for the detection of the corrosion of Al; b.) digital photographs of the "turn off" mechanism of the N-CDs in the presence of Al^{3+}.

Thus, we can utilize the quenching property of our synthesized N-CDs in the presence of Al^{3+} to devise a pH-paper like material which is very easy to manufacture as well as very efficient in the detection of the corrosion of the metal, before it is visible on the metal surface. We believe that it is a very practical approach to utilize N-CDs in order to detect the corrosion in metals as they exhibit quenching, so that necessary steps can be taken to prevent the metals from corroding further and maintain their property and application.

4. Conclusion

This study successfully demonstrates the synthesis and application of nitrogen-doped carbon dot/acrylic nanocomposite coatings *via* cathodic electrodeposition. The incorporation of N-CDs enhances the physical, mechanical, and anti-corrosive properties of the coatings by increasing adhesion, reducing porosity, and forming a passivation layer on the aluminium substrate. Electrochemical studies confirm that the Ac1NCD formulation significantly improves the corrosion resistance of the pristine acrylic coatings.

Besides protection, the fluorescence quenching behavior of N-CDs in response to Al^{3+} ions enables real-time corrosion monitoring. The development of a simple, visually detectable "turn-off" sensor provides an innovative and cost-effective method for detecting the initiation and progression of corrosion, offering practical implications for structural integrity assessment. These findings open avenues for the integration of functional nanomaterials in smart coatings, combining protection and early detection to extend the lifespan of metal components in harsh environments.

However, it should be mentioned that the pH-paper like corrosion sensor is a proof-of-concept and future work needs to be done in the direction of enhancing the LOD of the system which can be utilized to detect the corrosion at even earlier stages.

Data availability

The authors confirm that the data supporting the findings of this study are available within the article and in its ESI.† Also, data will be shared on request.

Author contributions

S. S.: conceptualization, methodology, formal analysis, validation, investigation, and writing. A. C.: investigation, validation, formal analysis, and writing. K. D.: formal analysis, and validation. S. B.: formal analysis and validation. P. K. M.: conceptualization, methodology, supervision, and editing.

Conflicts of interest

The authors declare no conflicts of interest. M/S SBL Specialty Coatings Pvt. Ltd., India declares no conflicts of interest with the article.

Acknowledgements

The authors SS, AC, KD, and SB express their gratitude to the Ministry of Education, Government of India for granting them fellowships to pursue their doctoral studies. We express our gratitude for the financial assistance provided by M/S SBL Specialty Coatings Pvt. Ltd., India.

References

1 *India loses 5-7% of GDP due to corrosion*, International Zinc Association, ET Auto, **https://auto.economictimes.indiatimes.com/news/industry/india-loses-5-7-of-gdp-due-to-corrosion-international-zinc-association/83390627**, (accessed 2023-11-10).

2 *The Global Cost and Impact of Corrosion*, **https://inspectioneering.com/news/2016-03-08/5202/nace-study-estimates-global-cost-of-corrosion-at-25-trillion-ann**, (accessed 2024-05-23).

3 L. Hamadi, S. Mansouri, K. Oulmi and A. Kareche, The Use of Amino Acids as Corrosion Inhibitors for Metals: A Review, *Egypt. J. Pet.*, 2018, **27**(4), 1157–1165, DOI: **10.1016/J.EJPE.2018.04.004**.

4 S. Sen, A. Chatterjee, D. Ramakanth, S. Singh and P. K. Maji, Recent Advances in Cathodic Electrodeposition Coatings with Special Reference to Resin Materials: A Comprehensive Review, *Prog. Org. Coat.*, 2024, **190**, 108387, DOI: **10.1016/J.PORGCOAT.2024.108387**.

5 Z. Gong, W. Zhao and L. Chen, Synthesis and Characterization of Cationic Acrylic Resin Used in Cathodic Electrodeposition Coatings, *J. Polym. Res.*, 2022, **29**(7), 303, DOI: **10.1007/s10965-022-03158-4**.

6 M. Haghi, Z. Ranjbar, H. Kazemian and M. Aghili, Synthesis, Characterization and Corrosion Resistance Behavior of Waterborne Cationic Acrylic Resins, *Prog. Color, Color. Coat.*, 2023, **16**(1), 31–45, DOI: **10.30509/pccc.2022.166897.1135**.

7 T. Wang, S. Qi, B. Ren and Z. Tong, Preparation and Surface Characteristics of Low-Temperature Curing Fluorinated Cathodic Electrodeposition Coating, *Prog. Org. Coat.*, 2007, **60**(2), 132–139, DOI: **10.1016/j.porgcoat.2007.07.009**.

8 T. Wang, S. Qi, B. Ren and Z. Tong, Low-Temperature Curing of Water-Dispersible Cationic Diisocyanates for Cathodic Electrodeposition Coatings, *J. Appl. Polym. Sci.*, 2008, **107**(6), 4036–4042, DOI: **10.1002/app.27627**.

9 Z. Gong and L. Chen, Preparation of Fluorine and Silicon Modified Cationic Acrylic Resin and Its Application in Cathodic Electrodeposition Coatings, *Pigm. Resin Technol.*, 2024, **53**(6), 710–715, DOI: **10.1108/PRT-08-2022-0096**.

10 L. Chen, W. Li and W. Jiang, Synthesis and Application of Cationic Fluorinated Acrylic Resin for Use in Cathodic Electrodeposition Coatings, *Pigm. Resin Technol.*, 2014, **43**(5), 251–255, DOI: **10.1108/PRT-10-2013-0093**.

11 S. V. Harb, M. S. Rodrigues, T. A. C. de Souza, A. Trentin, M. C. Uvida, D. J. Pochapski, S. H. Pulcinelli, C. V. Santilli and P. Hammer, Smart PMMA-cerium Oxide Anticorrosive Coatings: Effect of Ceria Content on Structure and Electrochemical Properties, *Prog. Org. Coat.*, 2021, **161**, 106548, DOI: **10.1016/J.PORGCOAT.2021.106548**.

12 S. Pourhashem, F. Saba, J. Duan, A. Rashidi, F. Guan, E. G. Nezhad and B. Hou, Polymer/Inorganic Nanocomposite Coatings with Superior Corrosion Protection Performance: A Review, *J. Ind. Eng. Chem.*, 2020, **88**, 29–57, DOI: **10.1016/J.JIEC.2020.04.029**.

13 O. D. Lewis, G. W. Critchlow, G. D. Wilcox, A. Dezeeuw and J. Sander, A Study of the Corrosion Resistance of a Waterborne Acrylic Coating Modified with Nano-Sized Titanium Dioxide, *Prog. Org. Coat.*, 2012, **73**(1), 88–94, DOI: **10.1016/J.PORGCOAT.2011.09.004**.

14 H. Zhou, Q. Lu, Z. Su, A. Zhou, X. Chen, B. Zhang, F. Qi, N. Zhao and X. Ouyang, Study on Anticorrosive and Self-Healing Properties of Acrylic Resin Modified with Nitrogen-Doped Carbon Quantum Dots, *Chem. Eng. J.*, 2024, **494**, 153165, DOI: **10.1016/J.CEJ.2024.153165**.

15 X. Wang, C. Li, M. Zhang, D. Lin, S. Yuan, F. Xu, Y. Zhou, C. Wang, Y. Zhu and H. Wang, A Novel Waterborne Epoxy Coating with Anti-Corrosion Performance under Harsh Oxygen Environment, *Chem. Eng. J.*, 2022, **430**, 133156, DOI: **10.1016/J.CEJ.2021.133156**.

16 A. Madhi, Smart Epoxy/Polyurethane/Carbon Quantum Dots Hybrid Coatings: Synthesis and Study of UV-Shielding, Viscoelastic, and Anti-Corrosive Properties, *Polym.-Plast. Technol. Mater.*, 2023, **62**(4), 403–418, DOI: **10.1080/25740881.2022.2116342**.

17 N. R. Dhongde, N. K. Das, T. Banerjee and P. V. Rajaraman, Synthesis of Carbon Quantum Dots from Rice Husk for Anti-Corrosive Coating Applications: Experimental and Theoretical Investigations, *Ind. Crops Prod.*, 2024, **212**, 118329, DOI: **10.1016/J.INDCROP.2024.118329**.

18 Z. Di, Q. Zhao, H. Xu, K. Wu, Y. Yan, X. Jin, H. Shen, Y. Lv and B. Ran, N-Doped Carbon Quantum Dots with Mechanical Enhancement and Fluorescence Properties Toward Anti-Corrosion Coating, *Int. J. Electrochem. Sci.*, 2022, **17**(12), 2212101, DOI: **10.20964/2022.12.102**.

19 Y. Song, C. Zhu, J. Song, H. Li, D. Du and Y. Lin, Drug-Derived Bright and Color-Tunable N-Doped Carbon Dots for Cell Imaging and Sensitive Detection of Fe^{3+} in Living Cells, *ACS Appl. Mater. Interfaces*, 2017, **9**(8), 7399–7405, DOI: **10.1021/ACSAMI.6B13954/ASSET/IMAGES/LARGE/AM-2016-13954D_0007.JPEG**.

20 S. Singh, S. Bhardwaj, R. S. Meda, C. Verma, M. Chhajed, K. Ghosh and P. K. Maji, Insights into Thermal Degradation Kinetics and Liquid Crystalline Behavior of Cellulose Nanocrystals from the Waste of Cajanus Cajan (Pigeon Pea), *Int. J. Biol. Macromol.*, 2023, **242**, 124507, DOI: **10.1016/J.IJBIOMAC.2023.124507**.

21 M. Zhu, L. Guo, Z. He, R. Marzouki, R. Zhang and E. Berdimurodov, Insights into the Newly Synthesized N-Doped Carbon Dots for Q235 Steel Corrosion Retardation in Acidizing Media: A Detailed Multidimensional Study, *J. Colloid Interface Sci.*, 2022, **608**, 2039–2049, DOI: **10.1016/J.JCIS.2021.10.160**.

22 J. Wang, P. Du, H. Zhao, J. Pu and C. Yu, Novel Nitrogen Doped Carbon Dots Enhancing the Anticorrosive Performance of Waterborne Epoxy Coatings, *Nanoscale Adv.*, 2019, **1**(9), 3443–3451, DOI: **10.1039/C9NA00155G**.

23 M. Jayasree, A. Asif, N. G. Pillai, K. Archana and G. T. Prakash, Development of Nitrogen Doped Carbon Dot (N-CDs) Encapsulated Zeolitic Imidazolate Framework-8 (N-CDs@ZIF-8), *Mater. Today: Proc.*, 2021, **41**, 564–569, DOI: **10.1016/J.MATPR.2020.05.250**.

24 Y. Qiang, S. Zhang, H. Zhao, B. Tan and L. Wang, Enhanced Anticorrosion Performance of Copper by Novel N-Doped Carbon Dots, *Corros. Sci.*, 2019, **161**, 108193, DOI: **10.1016/J.CORSCI.2019.108193**.

25 J.-J. Yin, F. Wahid, Q. Zhang, Y.-C. Tao, C. Zhong, L.-Q. Chu, J.-J. Yin, F. Wahid, Q. Zhang, Y.-C. Tao, L.-Q. Chu and C. Zhong, Facile Incorporation of Silver Nanoparticles into Quaternized Poly(2-(Dimethylamino)Ethyl Methacrylate) Brushes as Bifunctional Antibacterial Coatings, *Macromol. Mater. Eng.*, 2017, **302**(6), 1700069, DOI: **10.1002/MAME.201700069**.

26 L. E. Manring, D. Y. Sogah and G. M. Cohen, Thermal Degradation of Poly(Methyl Methacrylate). 3. Polymer with Head-to-Head Linkages, *Macromolecules*, 1989, **22**(12), 4652–4654, DOI: **10.1021/MA00202A048/ASSET/MA00202A048.FP.PNG_V03**.

27 S. Li, F. Du, Y. Lin, Y. Guan, W. J. Qu, J. Cheng and D. Wang, Excellent Anti-Corrosion Performance of Epoxy Composite Coatings Filled with Novel N-Doped Carbon Nanodots, *Eur. Polym. J.*, 2022, **163**, 110957, DOI: **10.1016/J.EURPOLYMJ.2021.110957**.

28 *ASTM D3359 Test Methods For Measuring Adhesion By Tape – Micom*, **https://www.micomlab.com/micom-testing/astm-d3359/**, (accessed 2024-09-12).

29 W. L. Chen and K. R. Shull, Hydrophilic Surface Coatings from Acrylic Block Copolymers, *Macromolecules*, 1999, **32**(19), 6298–6306, DOI: **10.1021/MA9818836/ASSET/IMAGES/MEDIUM/MA9818836E00008.GIF**.

30 H. Yildirim Erbil and C. Elif Cansoy, Range of Applicability of the Wenzel and Cassie-Baxter Equations for Superhydrophobic Surfaces, *Langmuir*, 2009, **25**(24), 14135–14145, DOI: **10.1021/LA902098A/SUPPL_FILE/LA902098A_SI_001.PDF**.

31 L. R. Evans and W. C. Fultz, Tread Compounds with Highly-Dispersible Silica, *Rubber World*, 1998, **219**(2), 38–44.

32 K. Dev, S. Singh, S. Bhardwaj, P. Kukreti, D. Ramakanth, P. Kumar, S. Saini, P. Roy, V. C. Srivastava, K. Ghosh and P. K. Maji, Solvent-Selective Fluorescence Sensing of Mg^{2+} and Al^{3+} Ions by Pincer-Type NNO Schiff Base Ligand: An Experimental and DFT Optimized Approach, *Chem. – Eur. J.*, 2024, **30**(65), e202403256, DOI: **10.1002/CHEM.202403256**.

33 A. M. Aslandaş, N. Balci, M. Arik, H. Şakiroğlu, Y. Onganer and K. Meral, Liquid Nitrogen-Assisted Synthesis of Fluorescent Carbon Dots from Blueberry and Their Performance in Fe^{3+} Detection, *Appl. Surf. Sci.*, 2015, **356**, 747–752, DOI: **10.1016/J.APSUSC.2015.08.147**.

34 Z. Liu, R. Jia, F. Chen, G. Yan, W. Tian, J. Zhang and J. Zhang, Electrochemical Process of Early-Stage Corrosion Detection Based on N-Doped Carbon Dots with Superior Fe^{3+} Responsiveness, *J. Colloid Interface Sci.*, 2022, **606**, 567–576, DOI: **10.1016/J.JCIS.2021.08.058**.

35 S. K. Kailasa, S. Ha, S. H. Baek, L. M. T. Phan, S. Kim, K. Kwak and T. J. Park, Tuning of Carbon Dots Emission Color for Sensing of Fe3+ Ion and Bioimaging Applications, *Mater. Sci. Eng., C*, 2019, **98**, 834–842, DOI: **10.1016/J.MSEC.2019.01.002**.

36 T. K. Rout and A. V. Gaikwad, In-Situ Generation and Application of Nanocomposites on Steel Surface for Anti-Corrosion Coating, *Prog. Org. Coat.*, 2015, **79**(C), 98–105, DOI: **10.1016/J.PORGCOAT.2014.11.006**.

37 M. Bozorg and A. Ramezani, Characterization and Protective Performance of Acrylic-Based Nanocomposite Coating Reinforced with Silica Nanoparticles, *Mater. Corros.*, 2017, **68**(7), 725–730, DOI: **10.1002/MACO.201609347**.

38 U. Eduok, J. Szpunar and E. Ebenso, Synthesis and Characterization of Anticorrosion Zirconia/Acrylic Nanocomposite Resin Coatings for Steel, *Prog. Org. Coat.*, 2019, **137**, 105337, DOI: **10.1016/J.PORGCOAT.2019.105337**.

39 R. Aboorvakani, S. J. Kennady Vethanathan and K. U. Madhu, Influence of Zn Concentration on Zinc Oxide Nanoparticles and Their Anti-Corrosion Property, *J. Alloys Compd.*, 2020, **834**, 155078, DOI: **10.1016/J.JALLCOM.2020.155078**.

40 S. V. Harb, A. Trentin, T. A. C. de Souza, M. Magnani, S. H. Pulcinelli, C. V. Santilli and P. Hammer, Effective Corrosion Protection by Eco-Friendly Self-Healing PMMA-Cerium Oxide Coatings, *Chem. Eng. J.*, 2020, **383**, 123219, DOI: **10.1016/J.CEJ.2019.123219**.

41 S. M. Gad, X. Zhou, S. B. Lyon and S. Emad, Inhibition Mechanism of Anticorrosion Pigments Leached from Organic Coatings: Comparison between Salt Spray and Immersion Testing, *Prog. Org. Coat.*, 2023, **174**, 107266, DOI: **10.1016/J.PORGCOAT.2022.107266**.

42 A. Chatterjee, S. Sen, S. Singh, S. Bhardwaj and P. K. Maji, Corrosion Protection of Mild Steel via Cerium Nitrate Loaded Acrylic-Vinyl Polysilazane Based Hybrid Coatings, *Prog. Org. Coat.*, 2024, **197**, 108831, DOI: **10.1016/J.PORGCOAT.2024.108831**.

43 C. Zhu, Y. Fu, C. Liu, Y. Liu, L. Hu, J. Liu, I. Bello, H. Li, N. Liu, S. Guo, H. Huang, Y. Lifshitz, S.-T. Lee, Z. Kang, C. Zhu, Y. Fu, C. Liu, Y. Liu, L. Hu, J. Liu, I. Bello, H. Li, N. Liu, S. Guo, H. Huang, Y. Lifshitz, S. Lee and Z. Kang, Carbon Dots as Fillers Inducing Healing/Self-Healing and Anticorrosion Properties in Polymers, *Adv. Mater.*, 2017, **29**(32), 1701399, DOI: **10.1002/ADMA.201701399**.